Heliyon 10 (2024) e32319

Contents lists available at ScienceDirect

Heliyon

journal homepage: www.cell.com/heliyon

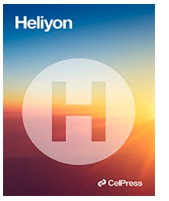

Research article

Anti-icing performance of hydrophobic coatings on stainless steel surfaces

Han Wang, Pinlu Cao, Shaotao Xu, Guoqing Cui, Zhuo Chen, Qilei Yin *

College of Construction Engineering, Jilin University, Changchun, 130021, China

ARTICLE INFO

Keywords:
Hydrophobic organic coatings
Anti-Icing performance
Ice adhesion strength
Ice drilling
Warm ice

ABSTRACT

This study aims to prevent ice accumulation on the surface of drilling tools by investigating the effectiveness of hydrophobic coatings, which is one of the most promising methods to solve drilling difficulties in warm ice. Herein, four types of hydrophobic organic coatings that can be used on metal surfaces were tested to evaluate their anti-icing performance, service durability, and friction properties. All of them possess rough surfaces with microstructure characteristics such as pores, stripes, or micropapillae. They also exhibit hydrophobicity, with water contact angles of 101.6°, 100.0°, 103.1°, and 108.5°. They can significantly prolong the required freezing time of water droplets on their surfaces, effectively reduce ice adhesion, and decrease the friction between ice and their surface. The ice adhesion in the axial, tensile, and tangential directions can be reduced by 65.64 %, 56.31 %, and 72.11 %, respectively, for the coating with silicon (Si)-based and fluorine (F)-containin compounds (coating-*C*) at −30 °C; while it can be reduced by 85.05 %, 73.9 %, and 94.2 %, respectively, for the coatings with Si-based and polytetrafluoroethylene (PTFE) compounds (coating-*D*). The two coatings mentioned above lose their anti-icing performance after 20 icing and de-icing cycles, and their hydrophobicity after 120 abrasion cycles under a load of 6 N.

1. Introduction

Icing, a natural phenomenon, poses challenges and risks in various industries and sectors. For example, power lines, aircraft, marine vessels and wind turbines are all susceptible to the negative effects of ice accumulation [1–3]. The accumulation of ice on electric power lines causes a flashover of insulator strings, resulting in power outages or structural damage (such as the collapse of towers). Additionally, the accretion of ice on wind turbine blades inhibits their optimal power performance, affecting their efficiency and safety during operation. In aircraft, ice formation on the wings or leading edges can alter the aerodynamic characteristics, resulting in serious malfunctions or disastrous consequences. In drilling tools, ice accumulation hinders their penetration rate, decreases drilling efficiency in ice core drilling, and can lead to drill-stuck incidents and tool losses [4]. Thus, addressing the problems caused by icing has become crucial in various fields, necessitating the development of effective solutions.

Generally, ice cores serve as invaluable resources for understanding the global climate history, geological evolution of the Earth, and glaciological dynamic behavior [5–7]. Given the urgency of understanding global warming and climate change, the retrieval of ancient ice cores from deep ice sheets has emerged as a critical objective in polar scientific research. Currently, electromechanical drills are commonly used for ice drilling to obtain ice cores due to their lightness and maneuverability [4]. However, drilling in so-called

* Corresponding author.
E-mail address: yinqilei@jlu.edu.cn (Q. Yin).

https://doi.org/10.1016/j.heliyon.2024.e32319
Received 8 March 2024; Received in revised form 21 April 2024; Accepted 31 May 2024
Available online 1 June 2024

"warm ice" (ice temperatures of −10 to 0 °C), which has a low melting point and poor drillability, presents significant challenges [8]. Ice chips produced during drilling are likely to melt or partially melt because of the cutting heat when the ambient temperature is close to their corresponding melting point. Subsequently, these chips can easily refreeze and adhere to the cutters of the drill bit, thereby blocking the circulation of the drilling fluid and reducing the penetration rate [9,10]. Moreover, refrozen ice between the drill bit and borehole wall can lead to a stuck drill bit, causing serious drilling incidents. Therefore, the icing phenomenon in ice drilling can significantly affect the drilling and coring processes, resulting in severe economic losses and environmental hazards [11].

In recent years, considerable attention has been directed towards solving the problems of ice accumulation on drilling tools in warm ice drilling, such as using ethanol-water solutions to dissolve the refrozen ice, altering the cutter structure and shape to reduce cutting heat or generate coarse ice chips, and raising the pump flow rate to improve its capacity to transport ice chips. However, despite the progress made, each method has its own shortcomings and limitations, highlighting the need for further improvements and advancements. For example, ethanol-water solutions have been successfully applied at ice drilling sites in NorthGRIP, EPICA Dome C, and EPICA Droning Maud Land. Nevertheless, it was found that the ice cores were also partially dissolved, resulting in poor quality [12]. Moreover, clathrate hydrates can be formed in the borehole if the drilling fluid contains a denaturant of HCFC 141b, which might negatively affect drilling safety [13]. Furthermore, in an attempt to address the challenges of warm ice drilling, a slotted cutter with a dihedral shape on its bottom surface was used in Hole No. 5 at Vostok Station, Antarctica. Despite the improved run length, the penetration rate was still low, and the applicability was poor [14]. In addition, ice drilling at the NEEM and Vostok stations used staggered cutters to solve the problems of warm ice drilling [15]. Although the coarse ice chips that it produces were less viscous and easier to transport from the borehole bottom, the penetration rate did not greatly increase, as expected [16,17]. Therefore, drilling difficulties in warm ice are far from solved when using electromechanical drilling tools, notwithstanding the above-cited efforts.

Researchers have explored the application of special organic coatings to solve the problems of ice accretion on drilling tools. In Dome Fuji, Antarctica, a special short Teflon-coated bit was successfully implemented, enhancing the drilling performance in warm ice conditions. Although its effect was temporary, this coating method improved the anti-icing performance of the drilling tool by preventing ice from adhering to its surface [18]. Later, a Teflon-coated dolphin holder was adopted for warm ice drilling at Aurora Peak in central Alaska [19]. The Teflon coating was effective in reducing the formation of ice on the drilling tool surfaces. Furthermore, a previous study investigating the anti-icing performance of four different hydrophobic coatings found that the ice-adhesion strength was significantly reduced on both flat and curved surfaces [4]. The use of anti-icing coatings to prevent ice formation and adhesion on the surface of drilling tools has become one of the most promising approaches for solving the problems of drilling in warm ice.

So far, hydrophobic and superhydrophobic organic coatings have been successfully used for the reduction of ice formation and accumulation in many fields, such as electric power transmissions, wind turbines, aeronautics, and marine vessels [20–22]. Previous studies have demonstrated that hydrophobic or superhydrophobic coatings can reduce ice adhesion on the material surfaces and prolong the freezing time of water droplets [23–25]. The reasons for this are related to the chemical composition and surface morphology of the coatings. Fluorine (F)-containing or silicon (Si)-based compounds are commonly utilized to fabricate hydrophobic coatings due to their lower surface energy [26–31]. They can form hydrophobic or superhydrophobic surfaces [32–35], reducing the contact area between the material and water droplets and making it easier for water droplets to roll off the material surface [36–38]. Thus, ice nucleation is prevented, reducing the ice cover on the material surface or even completely avoiding its formation. For example, the ice adhesion strength on the surface of a hydrophobic coating containing polytetrafluoroethylene (PTFE) was reduced by approximately 60 % [32]. The ice adhesion force in the shear direction on the organosilicon coating surface was only approximately 30 kPa, which is far less than that on the uncoated surface [21]. Compared to the chemical composition, the surface morphology of the coatings also plays an essential role in reducing ice adhesion [36]. Water droplets can only penetrate the micron-scale grooves but not the nanoscale folds on the rough surface of the coating. As a result, there are trapped air pockets in these nanoscale folds that remain when freezing occurs [39]. These trapped air pockets will significantly reduce the contact area between the ice and the material surface, resulting in a considerable decrease in ice adhesion, prolonging the freezing time of water droplets, and achieving anti-icing and de-icing effects.

Notably, although many types of commercially hydrophobic organic coating materials are available, most studies investigated their performance on aluminum alloys, wood, plastics, or glass, while fewer studies were conducted on stainless steel surfaces [40–42]. In this study, four commercially available hydrophobic organic materials were selected for use on a 304 stainless steel substrate to form a hydrophobic surface because most electromechanical drill tools are made of 304 stainless steel. The chemical composition, surface morphology, wettability and thermophysical property of each coating surface were characterized using Fourier transform infrared spectroscopy (FTIR), scanning electron microscopy (SEM), water contact angle measurements and thermal conductivity measurement. The anti-icing performance was evaluated by measuring the freezing time of the water droplets and the ice adhesion forces on the substrate surface at different temperatures. In addition, icing/de-icing and mechanical abrasion resistance tests were performed to investigate the service life of each coating during application. To ascertain the potential influence of chemical composition and coating surface smoothness on the transport of ice chips in drilling, the friction between the ice and the coating surface was examined by a series of friction tests.

2. Materials and methods

2.1. Materials

Table 1 lists the four types of commercially available hydrophobic organic coatings tested in this study. All of these coatings can easily adhere to metal substrates to form a hydrophobic surface through brushing. Thus, the use and maintenance of these coatings are

very convenient, even in remote regions such as the Arctic and Antarctica. The substrate material adopted was stainless steel 304 since most of the drilling tools used in polar regions are made from this material, as discussed above. Before applying the coatings, all substrate surfaces were fully polished and cleaned with an alcohol solution to ensure a consistent surface finish. After brushing, all four coating surfaces needed to be dried separately for subsequent testing, with the following detailed requirements: coating-*A* at 150 °C for 15 min, coating-*B* at 170 °C for 30 min, coating-*C* at 110 °C for 15 min, and coating-*D* at 200 °C for 30 min.

2.2. Analytical methods

Because the physical and chemical characteristics of the coated surfaces are important for the anti-icing performance of the hydrophobic surface, as mentioned above, the chemical composition, surface morphology, wettability and thermophysical properties of four hydrophobic coatings were investigated in the present study.

2.2.1. FTIR analysis

FTIR analysis was conducted to identify the functional groups of each coating for determining the chemical compositions of the four hydrophobic coatings. A Nicolet iS10 FTIR spectrometer (Thermo Nicolet, USA) was used to record the IR spectra of each sample. Each specimen for IR detection was a thin slice, which was prepared by pressing the mixture of the sample and potassium bromide or KBr powder at a mass ratio of 1:100. To obtain a good signal-to-noise ratio, all samples were recorded ranging from 4000 to 400 cm^{-1} with a resolution of 4 cm^{-1} and 16 scans.

2.2.2. SEM analysis

The surface morphology of the coatings was analyzed using a tungsten filament SEM (JSM-IT500, Japan). Before SEM analysis, a thin layer of gold was spattered on all specimens to ensure that all surfaces were sufficiently conductive for proper SEM imaging. An accelerating voltage of 10 kV was used for the analysis.

2.2.3. Water contact angle measurement

The wettability of a material is generally evaluated based on the water contact angle between a water droplet and a solid surface. In this study, the water contact angle of each coating was measured using a DSA-100 water droplet shape analyzer (Krüss, Germany) at room temperature (approximately 22 °C). Water droplets with a volume of approximately 2 μL are placed vertically on the surface of the samples. The shape of each water droplet was recorded using a high-speed camera. The water contact angle was then determined through image acquisition and data analysis via the DSA3 software. Each sample was measured five times, with the average taken as the final result.

2.2.4. Thermal conductivity measurement

The stainless steel specimens used in this experiment had dimensions of 50 mm in length, 40 mm in width, and 50 mm in height. Four hydrophobic coatings were applied to the surfaces of specimens according to the method described in section 2.1. The thermal conductivity was assessed at room temperature using a TPS 2500S Thermal Constant Analyzer (Hot Disk, Sweden). The probe code utilized was designated as K5501. The heating power was set at 1 W, and the duration of the test was established at 10 s. Prior to testing, the TPS 2500S was subjected to a standard calibration to ensure the accuracy of measurements. The TPS 2500S automatically recorded the thermal response data during the experiment. Five experiments were conducted with each specimen to ensure the reliability of the data. The experimental data were subsequently analyzed by specialized software to calculate the thermal conductivity of each coating.

2.3. Anti-icing performance tests

2.3.1. Freezing time test

A coating specimen 200 mm in length, 92 mm in width, and 5 mm in thickness was employed to characterize the ability of the four hydrophobic coatings to delay the freezing time of water droplets on their surfaces. Equal volumes of water droplets were injected at different locations on the specimen surface via a syringe. The freezing process of the water droplets was then recorded from a horizontal perspective using a high-speed camera. The time corresponding to the freezing process of water droplets on different coating surfaces can be ascertained by analyzing the attached video data.

Table 1
Four types of hydrophobic coatings used in this study.

Coating	Product	Composition	Manufacturer
A	M1502	Silicon (Si)-based compounds	Shenzhen Paiqi Nanotechnology Co., Ltd, China
B	Crystal Plating Solution	Fluorine (F)-containing compounds	Hanze New Material Trading Company, China
C	ZY220	Mixture of Si-based and F-containing compounds	Dongguan Changping Zhanrong Plastic Material Business Department
D	DS102	Mixture of Si-based and PTFE compounds	Dongguan Deshenglong Paint Co., Ltd., China

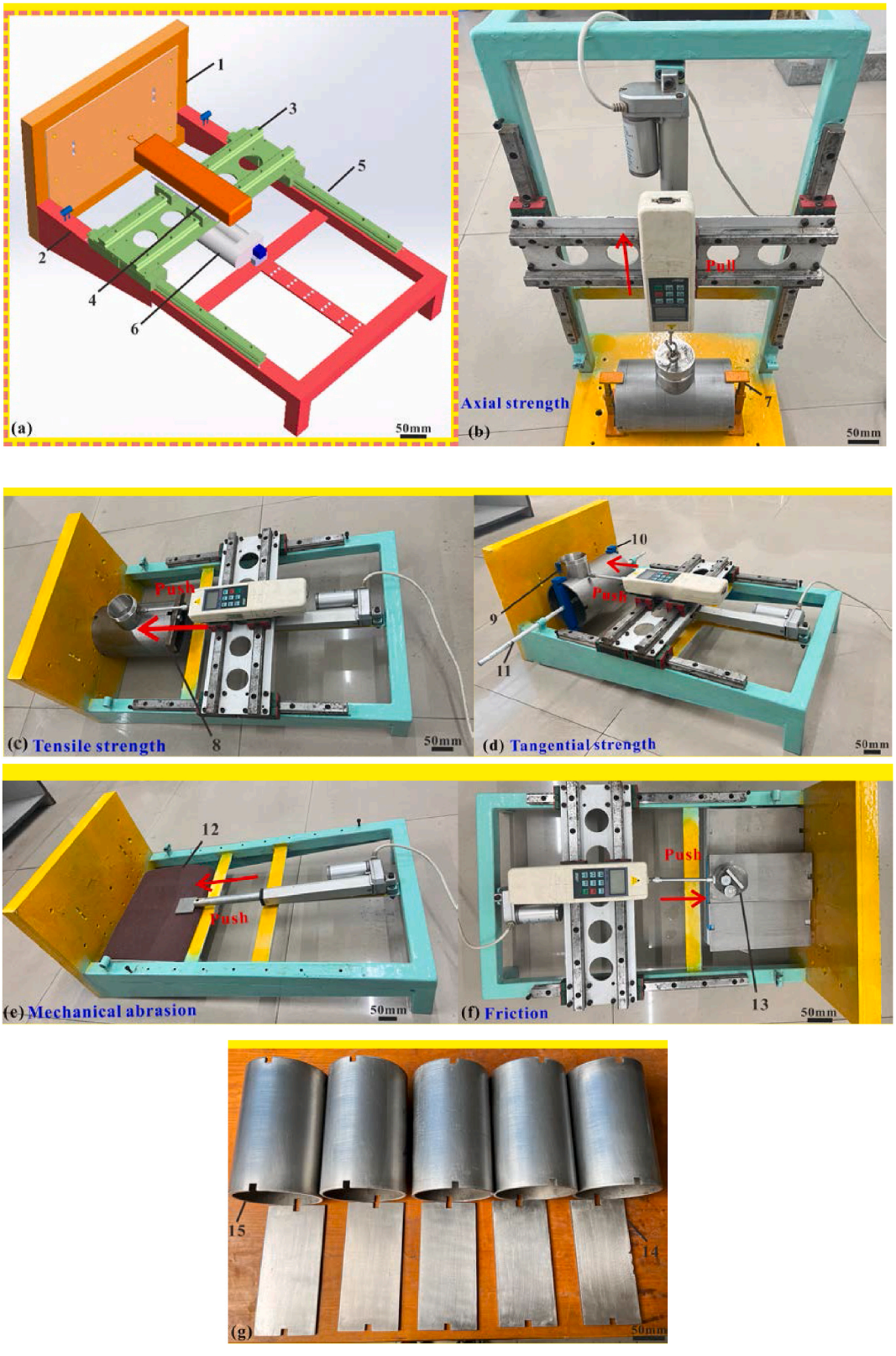

(caption on next page)

Fig. 1. Test setup of ice adhesion, coating durability and friction property: (a) schematic diagram, 1-base frame, 2-base frame, 3-guideway, 4-force gauge, 5-guideway, and 6-electric draw stem; **(b)–(d) tests for ice adhesion strengths in axial, tensile, and tangential directions,** 7-positioning device, 8-positioning device, 9-positioning device, 10-stainless-steel clips, and 11-stainless-steel center column; **(e) mechanical abrasion test** and 12-sandpaper; **(f) friction test** and 13-ice cube; and **(g) specimen,** 14-stainless-steel plate, and 15-stainless-steel tube.

2.3.2. Ice adhesion test

To investigate the ability of the hydrophobic coatings to prevent ice from adhering to the drilling tool surface, a special testing stand was designed, as shown in Fig. 1. It primarily comprises a base frame designed with two guideways, a positioning device, an electric putter, and a force gauge. Tubular coating samples with an outer diameter of 127 mm and thickness of 5 mm were positioned on the substrate plate of the base frame. A stainless-steel cylindrical sleeve with an inner diameter of 60 mm was placed on the coating specimen. Pre-cooled distilled water with a volume of approximately 40 mL was injected using a syringe. Because the water freezes immediately in the sleeve owing to its lower temperature, it was not necessary to seal the connection between the sleeve and the coating specimen. To ensure this, the distilled water was stored at a temperature close to 0 °C for at least 1 h. A stainless-steel cove was screwed on the top end of the sleeve. During testing, the electric putter moved along the guideways at a constant speed of 7 mm/s and pulled or pushed the steel through the cover to remove the ice from the interface between the ice and the coating samples. The maximum force applied to break the contact was measured and recorded by a force gauge. Then, the ice adhesion strength was obtained by calculating the force per contact area. To ensure the accuracy of the tests, an HF-3000 force gauge was used to record the peak forces with a measurement range of 0–3000 N and a precision of 1 N.

The entire experiment was carried out in a cold room with a temperature control between 0 and –30 °C. Before testing, the cylinder sleeve with the cover and the coating samples were kept in a cold room for several hours to avoid the influence of their initial temperature on the testing results. In addition, to ensure that the water was completely frozen, it was placed in a cold room and cooled for at least 4 h at a specific testing temperature. Five trials were conducted for each coating sample to reliably measure the mean and standard deviation of the testing results.

2.4. Durability tests

2.4.1. Icing/de-icing cycles tests

During the application of hydrophobic coatings, the surfaces undergo numerous icing and de-icing processes. Therefore, it is necessary to investigate the service life of hydrophobic coatings during icing/de-icing cycles to assess their durability. Because the tangential adhesion strength on the drilling tool surface plays a major role in ice drilling, the variation in the tangential adhesion strength during icing/de-icing cycle testing was evaluated. The experiments were conducted at −10 and −30 °C for de-icing and icing, respectively.

Notably, to prevent damage to the coating surface during the de-icing process, the coating specimen was placed at room temperature after each test to allow the ice to melt naturally. After the ice was completely removed, the coating specimens were placed in a cold room at the testing temperature for 4 h to ensure that their initial temperature had no impact on the ice properties before the next testing.

2.4.2. Mechanical abrasion resistance test

The coatings inevitably come in contact with the borehole wall during ice drilling, causing friction that may affect the durability and service life of the coatings. Moreover, the ice chips continually wipe the coating surfaces when transported to the ice chip chamber, also affecting the coating life. Therefore, it is important to evaluate the mechanical robustness of the coatings. Based on the study by Cao et al. [4], the method used to assess the mechanical robustness of each coating is described in Fig. 1.

The coating plate with a certain weight fixed on it was placed onto 2000 grit dry sandpaper, and then it was moved back and forth on the sandpaper using an electric draw stem. The speed and displacement of each movement were approximately 30 mm/s and 60 mm, respectively. After every 20 abrasion cycles, the water contact angle of each coating was measured to assess its mechanical abrasion resistance.

2.5. Friction property tests

In ice drilling, the friction between the ice chips and the drilling tool surface has a considerable effect on the movement of the ice chips. A large frictional value can increase the resistance of the ice chip motion, thereby affecting their transportation. This causes ice chips to accumulate near the drill bit, resulting in a drill-stuck incident. This is especially true for electromechanical drill tools that use spiral vanes to transport ice chips. Therefore, it is necessary to analyze the friction coefficient between the coating surface and ice.

The apparatus used to investigate the friction between the coating surfaces and ice is shown in Fig. 1. Rectangular hydrophobic coatings (200 mm in length, 92 mm in width, and 5 mm in thickness) were fixed on the bottom plate of the base frame. An ice cube with a smooth bottom surface was placed on the coating surface. An electric putter was used to drive the force gauge to push the ice cube in the horizontal direction at a constant speed of 7 mm/s. The friction between the ice cube and the coating surface was recorded in real-time using a force gauge. Then, the friction coefficient of the coating surface can be calculated using the following formula:

$$F_0 = \mu M_0 g$$

where, F_0 is the friction measured by the force gauge during the friction property tests, N; μ is the friction coefficient of the coating surface; M_0 is the mass of the ice cube, 233 g; and g is the gravity coefficient, taken as 9.8 N/kg.

3. Results and discussion

3.1. The physicochemical properties of the hydrophobic coatings

3.1.1. Chemical composition

The FTIR spectra of the four hydrophobic coatings are shown in Fig. 2. The results for coating-*A* show that apparent absorption peaks appear at 1007 and 807 cm^{-1}, corresponding to the antisymmetric and symmetric contraction peaks of the Si–O–Si and Si–O–C functional groups, respectively. This indicates that coating-*A* consists mainly of Si-based compounds. The C–F characteristic peaks in coating-*B* appear at 1261, 1105, and 1038 cm^{-1}, indicating that coating-*B* is composed mainly of fluorinated compounds. For coating-*C*, the asymmetric contraction peaks of CF_3 and Si–O–Si functional groups appear at 1278 and 1100 cm^{-1}, respectively, which means that the main components of coating-*C* are F-containing compounds and Si-based compounds. Similarly, the C–F peak can be observed at 1100 cm^{-1} in the results of coating-*D*, suggesting the presence of F-containing compounds.

Notably, all four hydrophobic coatings exhibited distinct C═O absorption peaks. They are specifically located at 1640 and 1612 cm^{-1} for coating-*A*; 1757, 1640, and 1620 cm^{-1} for coating-*B*; 1640 and 1618 cm^{-1} for coating-*C*; and 1638 and 1618 cm^{-1} for coating-*D*. Furthermore, all four hydrophobic coatings have a clear –OH absorption peak at 3000 to 3600 cm^{-1}, which may be caused by the physical adsorption of water. The above results demonstrate that the four hydrophobic coatings have different chemical compositions, which is consistent with those described in Table 1.

3.1.2. Surface morphology

Fig. 3 shows SEM images of the four hydrophobic coatings. As shown in Fig. 3(a), coating-*A* had a few small irregular bumps ranging from 1 to 3 μm in width. However, more bumps and rod-like ridges appeared on the surface of coating-*B*. The lengths of the two ridges were 267 and 300 μm. In addition, some bumps were embedded between them, as shown in Fig. 3(b). For coating-*C*, there is a

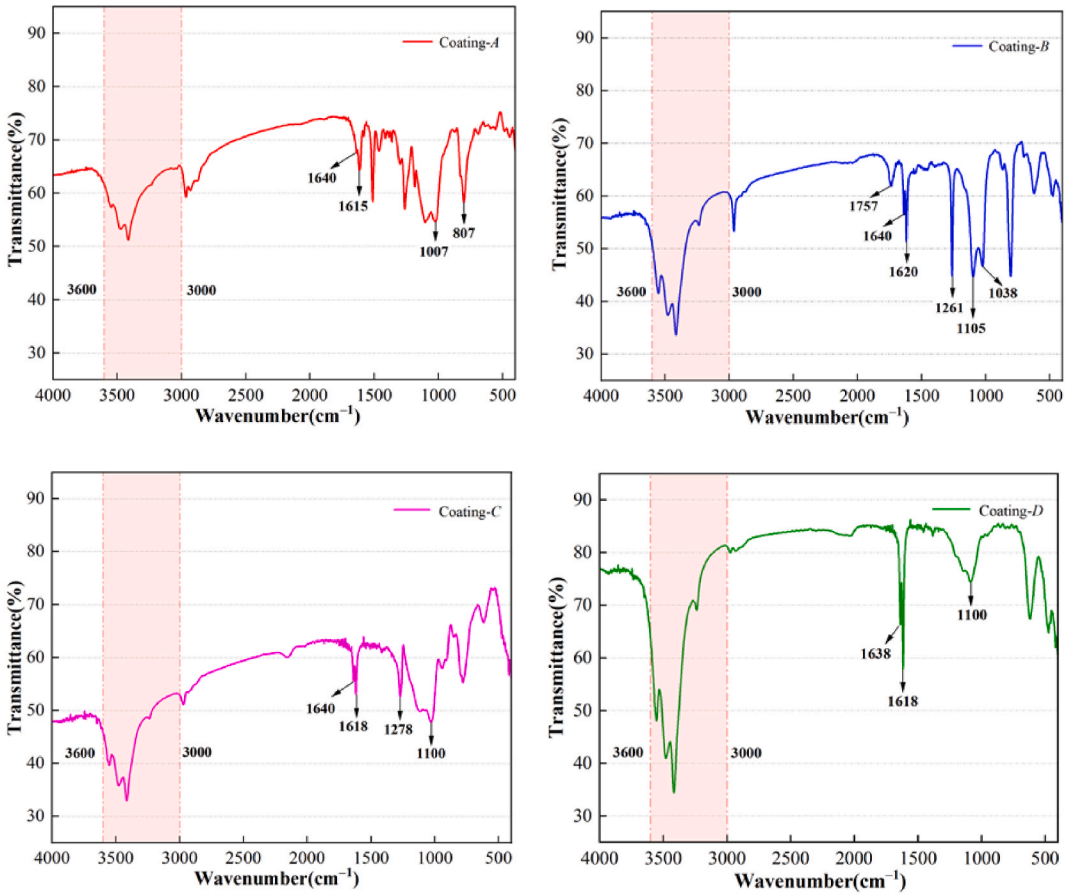

Fig. 2. The FTIR spectra of four hydrophobic coatings.

strip structure with micropapillae inside, and the width of the strip is approximately 21 μm, as presented in Fig. 3(c). The surface of coating-*D* exhibits a large number of irregular bumps, which cover approximately 70 % of the scanned area, as shown in Fig. 3(d). Inside these bumps, concave structures with a diameter of approximately 40 μm are found. In addition, the bumps also have a small area of duplex protrusion structure, which demonstrates a secondary composite structure. Moreover, it can be seen from Fig. 3 that coating-*D* has the highest rough area structure, followed by coating-*C*, while coating-*A* and -*B* have less.

Furthermore, all four hydrophobic coatings have rougher surfaces with the characteristics of microstructures such as porous, stripe, or micropapillae, which provide storage space for the adsorption of gas molecules. Therefore, in theory, they all have certain hydrophobic properties.

3.1.3. Wettability

The water contact angles of the uncoated and four different coatings are shown in Fig. 4. The contact angle is approximately 74.2° for the uncoated specimen surface, whereas it is 101.6°, 100.0°, 103.1°, and 108.5° for coating-*A*, -*B*, -*C*, and -*D*, respectively. Because the water contact angle values of all four hydrophobic coatings are greater than 90°, all of them exhibit obvious hydrophobicity. Moreover, their hydrophobic capacity can be arranged in the following order: coating-*D* > coating-*C* > coating-*A* > coating-*B*.

Notably, the above hydrophobic phenomena of the four coatings are related to their chemical composition and surface morphology. Generally, the lower the surface energy of a material, the better its hydrophobicity. According to the FTIR analysis results, all four hydrophobic coatings contained Si-based or F-containing compounds. F atoms have a strong electron-withdrawing capacity, so the surface energy of F-containing compounds is extremely low. For example, the surface energy of perfluoroalkyl is 10 mN/m. In addition, although Si has a high surface energy, it has a low interaction force with water molecules. Therefore, Si-based compounds also exhibit good hydrophobicity. Therefore, the hydrophobic properties of the four coatings are attributed to the fact that they all contain Si-based or F-containing compounds.

Moreover, based on the results of the SEM analysis, all four coatings have different surface roughness characteristics, as mentioned above, which can form air-insulating layers between the water droplets and the coating surfaces. Consequently, the water droplets are more likely to become spherical and thus roll off, contributing to their stronger hydrophobicity.

3.1.4. Thermophysical property

Fig. 5 presents the average values of thermal conductivity for uncoated specimen and specimens coated with four different coatings. The thermal conductivity of uncoated specimen is 14.38 W/(m·K), whereas the thermal conductivity of the specimens coated with coating-*A*, -*B*, -*C*, and -*D* decreases to 6.91, 6.27, 4.50, and 4.21 W/(m·K), respectively. These results obviously demonstrate that all

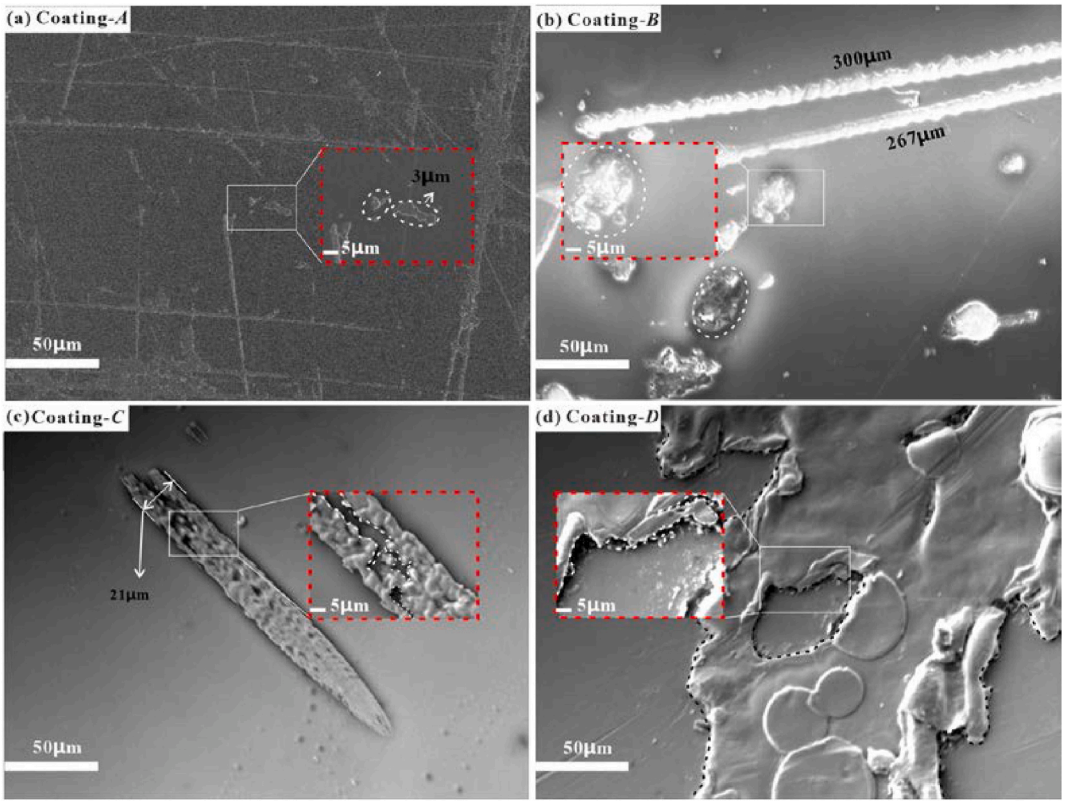

Fig. 3. The SEM images of four hydrophobic coatings.

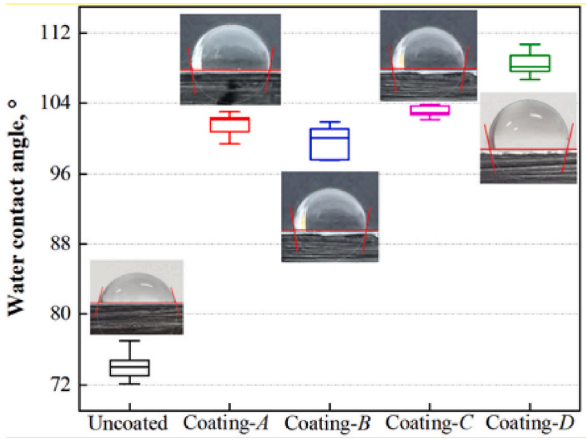

Fig. 4. Water contact angle on uncoated and coated specimen.

four coatings significantly reduce the thermal conductivity of the specimens. This reduction is primarily attributed to the inherently lower thermal conductivity of hydrophobic coatings containing Si-based or F-containing compounds compared to substrates such as stainless steel [43,44]. Additionally, the rough surface structure of the coatings, which harbors more air, not only reduces the contact area with water droplets but also further lowers the thermal conductivity [45]. Consequently, when applied to substrates like stainless steel with higher thermal conductivity, they lead to a reduction in the overall thermal conductivity of the structure. This reduction in thermal conductivity effectively decelerates the rate of heat transfer across the surface of the coatings.

3.2. Anti-icing performance of the hydrophobic coatings

3.2.1. Freezing time

Generally, one of the important indices for assessing the anti-icing performance of a coating is the time required for a water droplet to freeze [46,47]. Fig. 6 depicts the initial and final frozen shapes of water droplets on the uncoated surface and four hydrophobic coating surfaces at −10 °C. First, the water droplets are transparent, and then their shapes and transparency change continuously during the freezing process. When the transparency of the droplets no longer changes, the droplets display a peach-like shape, indicating that they are completely frozen [47].

The time required for a water droplet to freeze on various surfaces at different temperatures is shown in Fig. 7. It can be seen that it takes approximately 1.1 s for the water droplet to freeze into ice on the uncoated surface when the temperature is −30 °C. It takes approximately 4.5, 4.5, 8.3, and 8.5 s to freeze on the surfaces of coating-*A*, -*B*, -*C*, and -*D*, which means that the freezing time is prolonged by 309.1 %, 309.1 %, 654.5 %, and 672.7 %, respectively. In addition, the freezing time on all surfaces increased with an increase in the environmental temperature. As the temperature increased to −10 °C, the water droplets were completely frozen in 7.3 s on the uncoated surface. Meanwhile, about 15.8, 15.1, 27.1, and 29.5 s were required for the surfaces of coating-*A*, -*B*, -*C*, and -*D*, respectively, extending by 116.4 %, 106.8 %, 271.2 %, and 304.1 %. All four hydrophobic coatings delayed the freezing of water

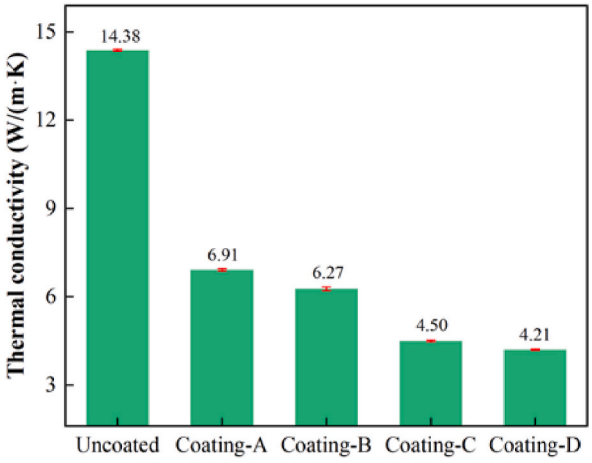

Fig. 5. The thermal conductivity of uncoated and coated specimen.

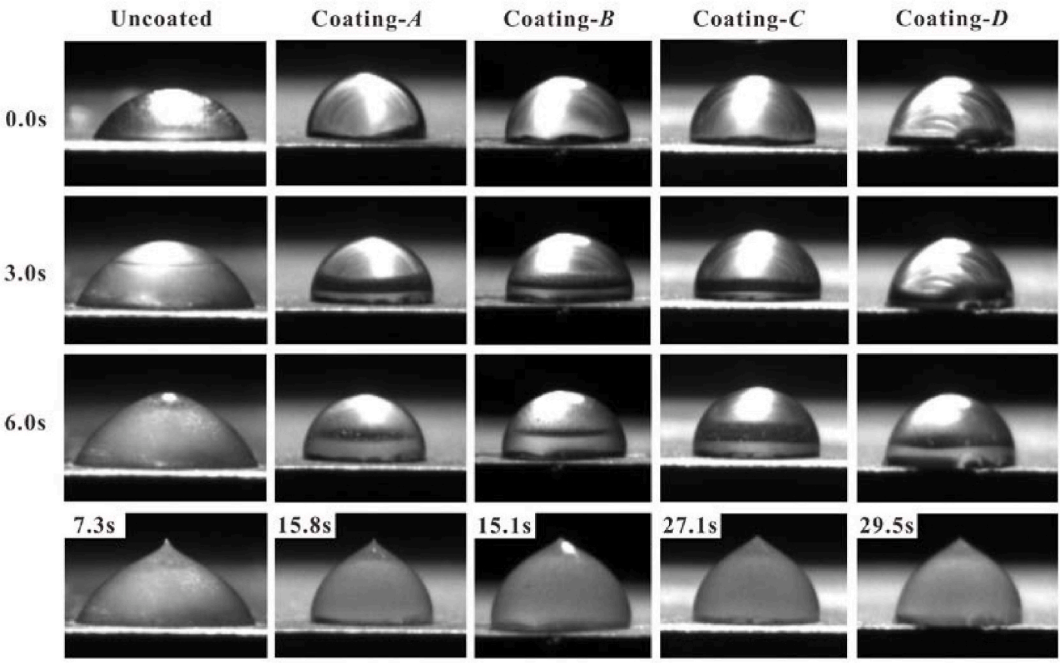

Fig. 6. The initial and final frozen shapes of water droplets at −10 °C.

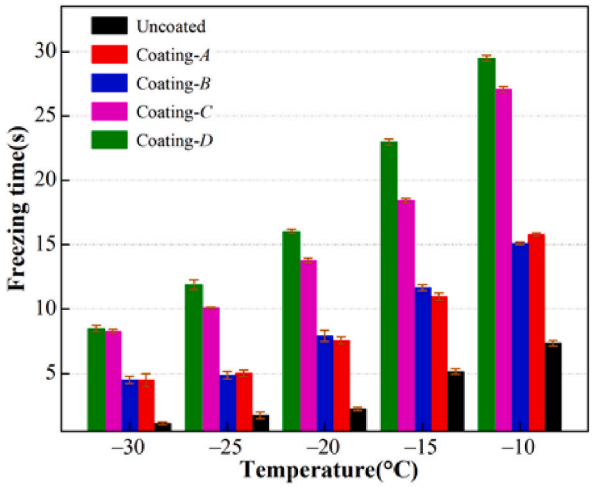

Fig. 7. Freezing time of water droplets on various surfaces at different temperatures.

droplets at any given temperature. Moreover, coating-*D* exhibited the best performance in delaying the freezing time of the water droplets, followed by coating-*C*, and coating-*B* was the worst. This effect can be attributed to several factors related to the composition and characteristics of the coatings. For one thing, the surface energy of hydrophobic coating is quite low, making the surfaces exhibit strong hydrophobicity to water. This results in a smaller contact area between the water droplets and the coated surfaces compared to uncoated steel, thereby limiting interfacial heat transfer and extending the freezing time [48]. Moreover, all four coatings significantly reduce the thermal conductivity of the specimens. Notably, coating-*C* and coating-*D* perform the best, followed by coating-*A* and coating-*B*. This reduction in thermal conductivity effectively decelerates the rate of heat transfer across the surface of the coatings, thus contributing to delaying the freezing process of the water droplets [49].

3.2.2. Ice adhesion strength

The ice adhesion strengths on different coating surfaces in the axial, tensile, and tangential directions at different testing temperatures are presented in Fig. 8. Evidently, all four hydrophobic coatings can effectively reduce ice adhesion compared to the uncoated coating. Moreover, the effects were more noticeable when the ambient temperature was lower. At −30 °C, the average axial

adhesion strength on the uncoated surface was 227 kPa, while it was reduced to 93.9, 90.4, 78.0, and 33.9 kPa on coating-*A*, -*B*, -*C,* and -*D* surfaces, respectively, which was minimized by 58.63 %, 60.18 %, 65.64 %, and 85.05 %, respectively, as shown in Fig. 8(a). When the ambient temperature increases to −10 °C, the average axial adhesion strength decreases to 115.2 kPa on an uncoated sample, while it was 63.2, 61.3, 44.3, and 84.2 kPa on coating-*A*, -*B*, -*C*, and -*D*, respectively, showing a decrease of 45.13 %, 46.79 %, 61.55 %, and 26.91 %. Thus, of the four hydrophobic coatings, coating-*C* and -*D* exhibited excellent anti-icing performance, while coating-*A* showed the worst anti-icing performance.

The variations in the tensile and tangential adhesion strengths of the different coatings exhibit similar trends to those of the axial adhesion strength, as shown in Fig. 8(b) and (c). All four hydrophobic coatings significantly reduced the tensile and tangential ice adhesion strengths. Among the four coatings, coating-*C* and -*D* displayed outstanding anti-icing performance. The coating-*D* performed best at lower temperatures, reducing the tensile and tangential adhesion strengths by 73.9% and 94.2% at −30 °C, respectively. The coating-*C* showed the best results at higher temperatures, which can decrease the tensile and tangential adhesion strengths to 66.3 kPa and 46.8 kPa at −10 °C, respectively.

Combined with the experimental results of ice adhesion strength, it is evident that all four coatings show a reduction in ice adhesion (in all three directions) compared to uncoated bare steel. Firstly, all four hydrophobic coatings contain components that significantly reduce the surface energy, such as Si-based or F-containing compounds. The low surface energy diminishes the mutual attraction between the ice and the coatings, thereby reducing ice adhesion [50]. Moreover, all four coatings have a certain degree of rough surface morphology, decreasing the contact area between water droplets and the coatings, which in turn reduces adhesion [51]. Additionally, the four coatings have lower thermal conductivity compared to bare steel, which slows down the temperature decrease on the coating surfaces under freezing conditions, minimizing the mechanical bonding between the ice and the surface by reducing the likelihood of ice melting and refreezing [49].

Notably, the above results indicate that the wettability of the material surface, that is, the water contact angle, does not simply correlate positively with the ice adhesion strength, which is consistent with the results of previous studies [52]. The water contact angle of coating-*A* is greater than that of coating-*B*, while its anti-icing performance is worse than that of coating-*B*. Coating-*C* has a lower water contact angle than coating-*D*, whereas it shows better anti-icing performance at higher temperatures.

In addition, the ambient temperature is a significant factor affecting the ice adhesion strength. As the temperature increases, the ice adhesion on coating-*A*, -*B,* and -*C* decreases, similar to the uncoated coating, showing an approximately positive correlation, which

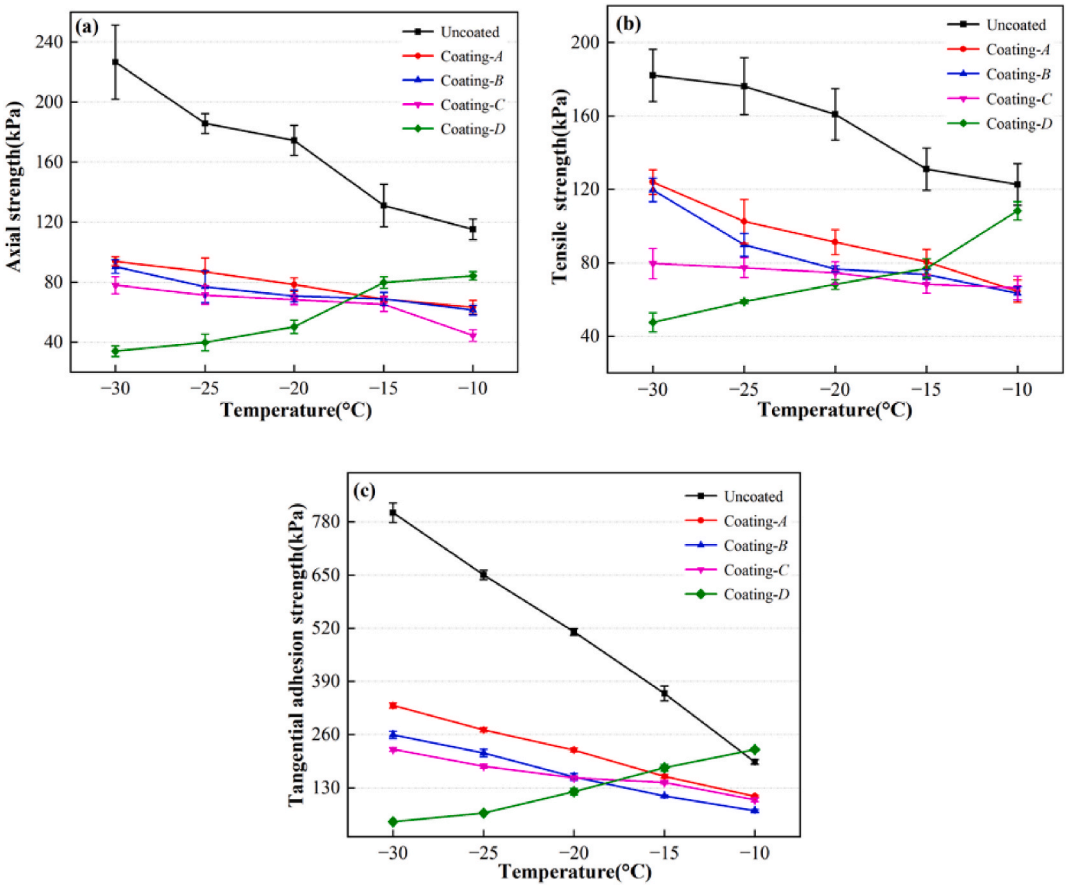

Fig. 8. The ice adhesion strengths on different coating surfaces in axial, tensile, and tangential directions at different testing temperatures.

exhibits the same trend as previous studies [53,54]. This is because as the temperature rises, the surface energy of the samples decreases [55], which has been demonstrated to lead to a decrease in ice adhesion [56]. However, coating-*D* shows an approximately negative correlation with temperature. Its anti-icing performance decreases with an increase in temperature at low temperatures, which is in accordance with previous studies [57]. For one thing, the freezing rate of water on the coating surface increases as the ambient temperature decreases [58]. This can result in the freezing of water into ice before it enters the microstructure at the coating surface, leaving a large amount of air between the ice and the coating surface. As a result, the actual contact area is reduced and the ice adhesion is lowered. Besides, as the temperature decreases, the hardness of PTFE increases. It may become more non-sticky and exhibit a more significant resistance to water adhesion, thereby reducing the ice adhesion [59].

3.3. Durability of the hydrophobic coatings

3.3.1. Service life

To gain a better understanding of the service life of each coating tested in this study, icing-de-icing tests were carried out, as discussed above. The variations in the tangential adhesion strength of ice adhered to different surfaces with different icing and de-icing cycles are shown in Fig. 9. Although hydrophobic coatings can significantly reduce ice adhesion strength and prevent ice accumulation, durability is the most difficult challenge for their practical applications. As shown in Fig. 9(a), the tangential adhesion strength exhibited an increasing trend as the number of icing/de-icing cycles increased. For coating-*A* and -*B*, the tangential adhesion strength increased to approximately 802.3 kPa after 10 icing/de-icing cycles at −30 °C, which is slightly higher than that on the uncoated surface (802.3 kPa). For coating-*C* and -*D*, the tangential adhesion strength was close to that on the uncoated surface after 20 cycles. Obviously, coating-*C* and -*D* have longer excellent service lives than the other two coatings at −30 °C, but they lose their anti-icing properties after 20 cycles.

Fig. 9(b) shows the variations in the tangential adhesion strength in 1–12 icing and de-icing cycles at −10 °C. Due to the poor anti-icing performance of coating-*D* at this temperature, its durability was not investigated in this study. Similarly, with repetitive icing and de-icing, all three coating samples exhibited gradually increased ice adherence. For coating-*A* and -*B*, the tangential forces reached about 201.6 and 195.5 kPa after 8 cycles, respectively, both exceeding the one on the uncoated surface (193.2 kPa). Meanwhile, coating-*C* still exhibited some anti-icing performance after 10 cycles.

According to previous reports on various hydrophobic and superhydrophobic surfaces, these increases in ice adhesion strength are attributed to a larger ice-solid contact area on these surfaces after several icing and de-icing tests [38]. During the icing process, ice crystals may form in microcracks, pores, or defects in the coating, causing deformation or even fracturing of the coatings. Moreover, the melted water during the de-icing process may penetrate the damaged areas of the coatings and form new ice nuclei, thereby increasing ice adhesion on the coating surfaces. Meanwhile, repeated icing and de-icing processes may also lead to changes in the chemical composition and structure of the coatings. For example, water molecules can react with the internal groups of the coatings, such as hydroxyl and carboxyl groups, to form hydrogen bonds, which increases the ice adhesion strength.

3.3.2. Mechanical abrasion resistance

The results of the water contact angle measurements on the four hydrophobic coating surfaces under different loads with various abrasion cycles are shown in Fig. 10(a)–(f). It shows that the water contact angle on the surface of all four hydrophobic coatings continuously decreases with an increase in the number of friction cycles under different loads. Coating-*C* and -*D* have the highest number of abrasion cycles, demonstrating excellent mechanical abrasion resistance, whereas, for coating-*A* and -*B*, their mechanical abrasion resistances are weak at any given load. This is probably due to the larger friction coefficients of coating-*A* and -*B*, which lead to higher friction under the same load. Thus, the microstructures of their surfaces are rapidly damaged, which accelerates the coating

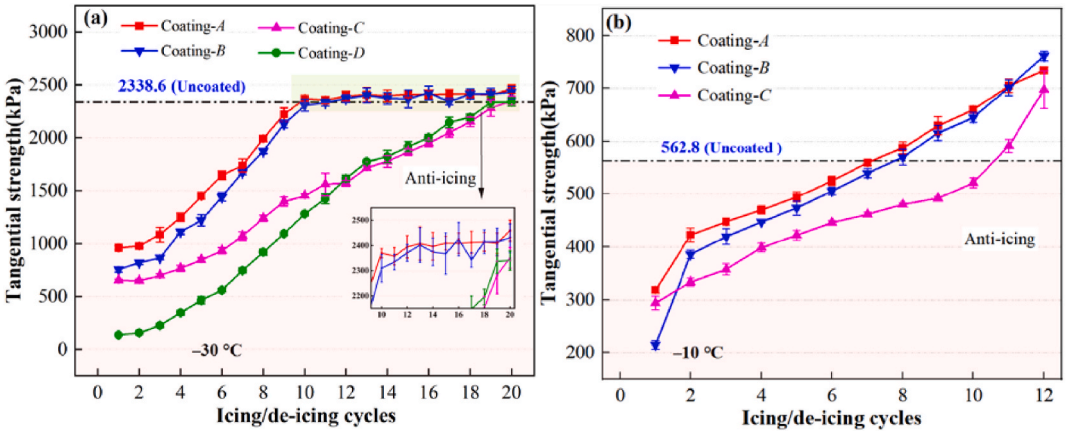

Fig. 9. The variations of tangential adhesion strength of ice adhesion on the different hydrophobic coating surfaces in the icing/de-icing cycles at (a) −30 °C and (b) −10 °C.

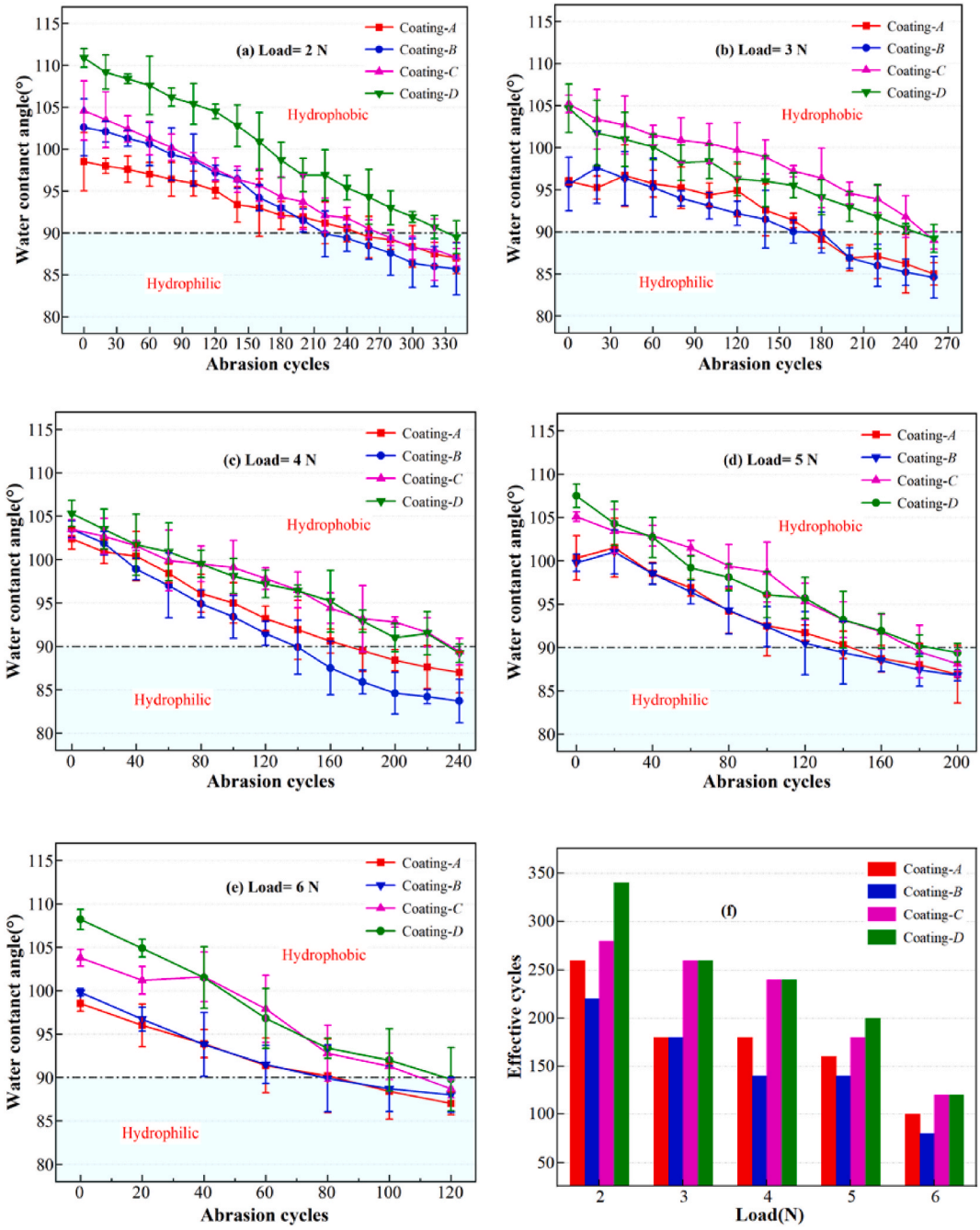

Fig. 10. The results of the water contact angle on the four hydrophobic coating surfaces under (a) 2, (b) 3, (c) 4, (d) 5, and (e) 6 N with various abrasion cycles. (f) The cycles corresponding to the loss of hydrophobicity for the four coatings under different loads.

failure. However, the surface microstructures were damaged more slowly owing to the smaller friction coefficients of coating-*C* and -*D*. Therefore, the corresponding mechanical abrasion resistances performed better. The friction coefficients of the four coatings will be discussed in detail later.

Based on the results of Figs. 9 and 10, although they have excellent anti-icing performance for coating-*C* and coating-*D*, they cannot bear a larger friction load. Hence, they may not be strong enough to be used on the cutters of the drill bit because large friction is generated between ice and the cutters during ice drilling. This needs to be further tested and analyzed. Even so, they can be used on other parts of the drill where no significant friction force is generated. Moreover, these two coatings are easily brushed onto the surfaces of drilling tools, making them convenient for use. Once the coating fails, it can be easily repaired in the drilling field. The real effectiveness of anti-icing in ice drilling needs further study.

Taken together, coating-*D* is more suitable for application at extremely low temperatures, such as −30 to −20 °C, whereas coating-*C* can be used in a wide range of low temperatures.

Fig. 11 illustrates the initial and final shapes after different abrasion cycles of water droplets on the four hydrophobic coating surfaces under a load of 6 N. The water contact angles of all four hydrophobic coatings were less than 90° after a certain number of abrasion cycles, indicating that they all lost their hydrophobicity to varying degrees.

3.4. Friction properties of the hydrophobic coatings

Fig. 12 illustrates the friction variation between the ice and coating surfaces at different temperatures. At an ambient temperature of −30 °C, the average friction force between the ice and the uncoated surfaces was 0.99 N, while it was reduced to 0.54, 0.51, 0.31, and 0.46 N for coating-*A*, -*B*, -*C*, and -*D*, respectively. When the ambient temperature increased to −10 °C, it decreased to approximately 0.40 N for the uncoated surface, while it was 0.20, 0.27, 0.13, and 0.17 N for coating-*A*, -*B*, -*C*, and -*D*, respectively, as shown in Fig. 12. Therefore, all four hydrophobic coatings can effectively decrease the friction between the ice and the coatings at any testing temperature, which is beneficial to ice chip transportation in ice drilling, as discussed above.

The friction coefficients μ of the different coating surfaces were calculated using the formula described in Section 2.5, with the results shown in Fig. 13. The friction coefficient was about 0.24, 0.22, 0.14, and 0.20 at −30 °C for coating-*A*, -*B*, -*C*, and -*D*, respectively, and it was reduced to about 0.09, 0.12, 0.06, and 0.07 as the ambient temperature increased to −10 °C. The friction coefficients of all surfaces decreased with an increase in ambient temperature. This is because the surface energy of the samples decreases as the temperature increases, whereas the lower surface energy of the surface usually has a lower friction coefficient [55]. In addition, when it moves on the surface of the samples, the ice at the contact will melt owing to the friction between them. A thin water film is formed, which can lubricate their movement, thus reducing the friction between them [60]. When the temperature increased, the thickness of the water film increased, and the lubrication effect was enhanced, thereby lowering the friction coefficient. Among the four coatings, coating-*C* had the lowest friction coefficient, followed by coating-*D*, while coating-*A* and coating-*B* had higher friction coefficients. This is probably due to the surface energy and morphology of these coatings.

4. Conclusions

(1) All four hydrophobic organic coatings exhibit a certain hydrophobicity, with water contact angles of 101.6°, 100.0°, 103.1°, and 108.5°. They can significantly delay the freezing time of water droplets on their surfaces. The time required for water droplets to freeze was approximately 15.8, 15.1, 27.1, and 29.5 s at a ambient temperature of −10 °C, while it took approximately 4.5, 4.5, 8.3, and 8.5 s when the environmental temperature decreased to −30 °C for coating-*A*, -*B*, -*C*, and -*D*, respectively.

(2) The four coatings can effectively reduce ice adhesion at any testing temperature. Compared with the uncoated one, the ice adhesion strength in the axial, tensile, and tangential directions can be reduced by 65.64 %, 56.31 %, and 72.11 % for the coatings with the mixture of Si-based and F-containing compounds (coating-*C*), while it can be reduced by 85.05 %, 73.9 %, and 94.2 % for the coatings with Si-based and PTFE compounds (coating-*D*), respectively.

(3) The anti-icing performance and water repellency of the four coatings gradually decreased with use. They lost anti-icing performance after 20 icing and de-icing cycles for the coating with a mixture of Si-based and F-containing compounds (coating-*C*), along with the coating with a mixture of Si-based and PTFE compounds (coating-*D*), while the other two coatings only sustain 10 cycles. In addition, they lost hydrophobicity after 120 abrasion cycles for the first two coatings.

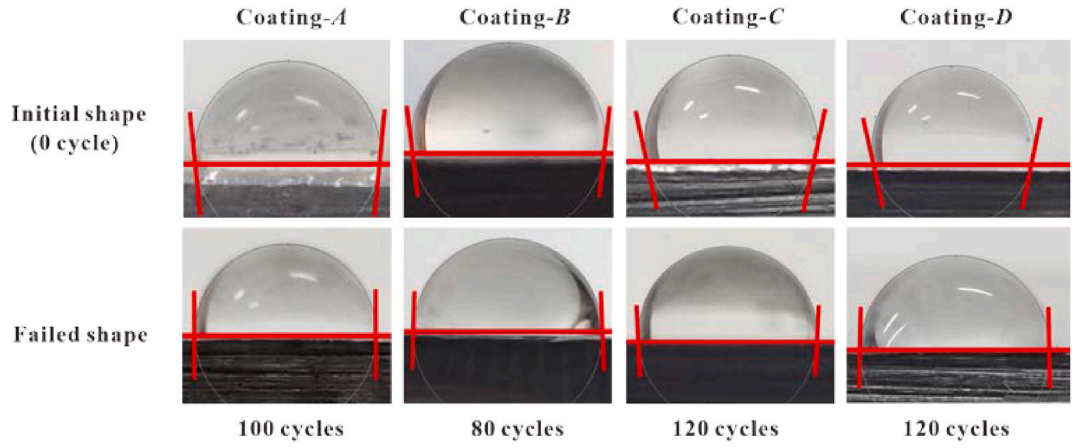

Fig. 11. The initial shapes and the final shapes after different abrasion cycles of water droplets on the four hydrophobic coating surfaces under a load of 6 N.

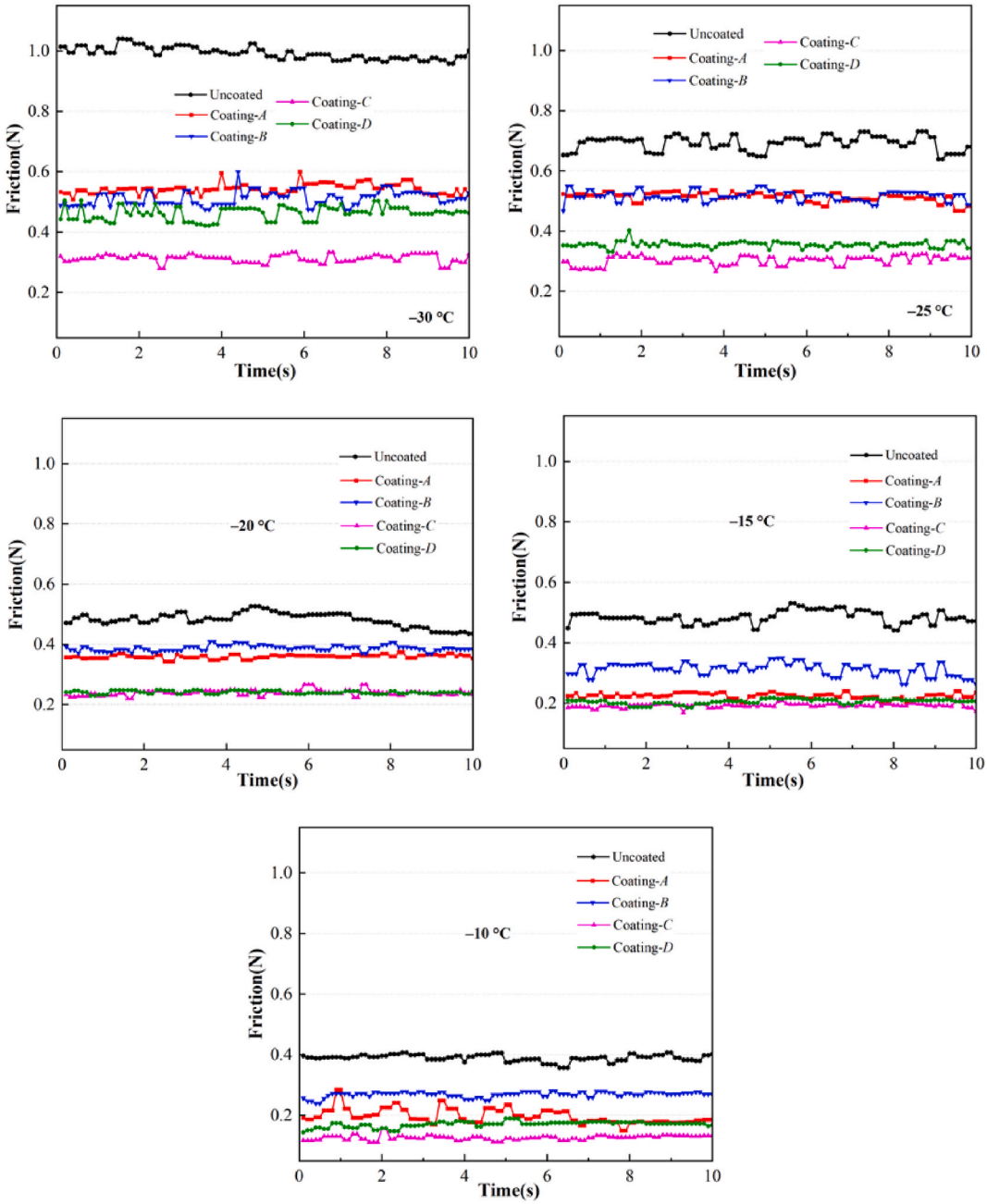

Fig. 12. The friction variation between the ice and the surfaces of the different specimens at different temperatures.

(4) All four coatings can effectively decrease the friction between the ice and their surface, which is beneficial to the transportation of ice chips in ice drilling. The friction coefficient is approximately 0.24, 0.22, 0.14, and 0.20, respectively, at −30 °C, and it will be reduced to approximately 0.09, 0.12, 0.06, and 0.07 as the ambient temperature increases to −10 °C.

(5) The hydrophobic coatings tested in this study have excellent anti-icing properties, which prolong the freezing time of water droplets and reduce ice adhesion, as well as demonstrating excellent durability and a low friction coefficient. Therefore, it is feasible to use the surface of electromechanical drill tools to prevent ice adhesion in warm ice drilling; however, this requires further study.

Data availability

Data will be made available on request.

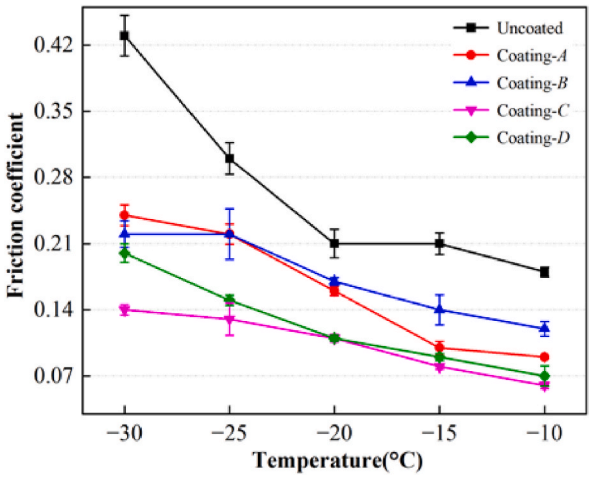

Fig. 13. The friction coefficients of different specimen surfaces at various temperatures.

CRediT authorship contribution statement

Han Wang: Writing – review & editing, Writing – original draft, Methodology, Investigation, Formal analysis, Data curation. **Pinlu Cao:** Writing – review & editing. **Shaotao Xu:** Writing – review & editing. **Guoqing Cui:** Supervision. **Zhuo Chen:** Supervision. **Qilei Yin:** Writing – review & editing, Supervision.

Declaration of competing interest

The authors declare that they have no known competing financial interests or personal relationships that could have appeared to influence the work reported in this paper.

Acknowledgements

The authors thank the anonymous reviewers and editors for their inspiring remarks and comments. This study was supported by the National Natural Science Foundation of China (Project No. 41976213).

References

[1] A. Ilinca, O. Parent, Anti-icing and de-icing techniques for wind turbines: critical review, Cold Reg. Sci. Technol. 65 (1) (2011) 88–96.
[2] Y.Z. Shen, H.J. Tao, S.L. Chen, L.M. Zhu, T. Wang, J. Tao, Icephobic/anti-icing potential of superhydrophobic Ti6Al4V surfaces with hierarchical textures, RSC Adv. 5 (3) (2015) 1666–1672.
[3] S.A. Kulinich, M. Farzaneh, Ice adhesion on super-hydrophobic surfaces, Appl. Surf. Sci. 255 (18) (2009) 8153–8157.
[4] P.L. Cao, Z. Chen, H.Y. Cao, et al., Anti-icing performance of hydrophobic material used for electromechanical drill applied in ice core drilling, J. Glaciol. 66 (258) (2020) 618–626.
[5] J. Beer, U. Siegenthaler, G. Bonani, R.C. Finkel, M. Suter, Information on past solar activity and geomagnetism from 10Be in the Camp Century ice core, Nature 331 (6158) (1988) 675–679.
[6] F. Steinhilber, J.A. Abreua, J. Beera, 9,400 years of cosmic radiation and solar activity from ice cores and tree rings, Proc. Natl. Acad. Sci. U.S.A. 109 (16) (2012) 5967–5971.
[7] P.L. Cao, B.Y. Chen, C.P. Liu, C. Yang, P. Talalay, Experimental investigation of cutting temperature in ice drilling, Cold Reg. Sci. Technol. 116 (2015) 78–85.
[8] V.M. Kotlyakov, V. Ya Lipenkov, N.I. Vasil'ev, Deep drilling in central Antarctica and penetration into subglacial Lake Vostok, Her. Russ. Acad. Sci. 83 (4) (2013) 311–322.
[9] F. Pattyn, Antarctic subglacial conditions inferred from a hybrid ice sheet/ice stream model, Earth Planet, Sci. Lett. 295 (3) (2010) 451–461.
[10] M. Truffer, R.J. Motyka, W.D. Harrison, K.A. Echelmeyer, B. Fisk, S. Tulaczyk, et al., Subglacial drilling at Black Rapids Glacier, Alaska, USA: drilling method and sample descriptions, J. Glaciol. 45 (151) (1999) 495–505.
[11] L. Augustin, H. Motoyama, F. Wilhelms, S. Johnsen, S.B. Hansen, P. Talalay, et al., Drilling comparison in 'warm ice' and drill design comparison, Ann. Glaciol. 47 (2007) 73–78.
[12] S.J. Johnsen, S.B. Hansen, S.G. Sheldon, D.D. Jensen, J.P. Steffensen, L. Augustin, et al., The Hans Tausen drill: design, performance, further developments and some lessons learned, Ann. Glaciol. 47 (2007) 89–98.
[13] M.M. Murshed, S.H. Faria, W.F. Kuhs, S. Kipfstuhl, F. Wilhelms, The role of hydrochlorofluorocarbon densifiers in the formation of clathrate hydrates in deep boreholes and subglacial environments, Ann. Glaciol. 47 (2007) 109–114.
[14] N.I. Vasiliev, P. Talalay, N.E. Bobin, V.K. Chistyakov, V.M. Zubkov, A.V. Krasilev, et al., Deep drilling at Vostok station, Antarctica: history and recent events, Ann. Glaciol. 47 (2007) 10–23.
[15] V. Zagorodnov, L.G. Thompson, P. Ginot, V. Mikhalenko, Intermediate-depth ice coring of high-altitude and polar glaciers with a lightweight drilling system, J. Glaciol. 51 (174) (2005) 491–501.
[16] T.J. Popp, S.B. Hansen, S.G. Sheldon, P. Christian, Deep ice-core drilling performance and experience at NEEM, Greenland, Ann. Glaciol. 55 (68) (2014) 53–64.
[17] P. Talalay, C. Yang, P.L. Cao, R.S. Wang, N. Zhang, X.P. Fan, et al., Ice-core drilling problems and solutions, Cold Reg. Sci. Technol. 120 (2015) 1–20.
[18] H. Motoyama, The second deep ice coring project at Dome Fuji, Antarctica, Sci. Rep. 5 (2007) 41–43.
[19] S. Matoba, K. Shimbori, T. Shiraiwa, Alpine ice-core drilling in the North Pacific region, Ann. Glaciol. 55 (68) (2014) 83–87.

[20] A. Chaudhary, H.C. Barshilia, Nanometric multiscale rough CuO/Cu (OH) (2) superhydrophobic surfaces prepared by a facile one-step solution-immersion process: transition to superhydrophilicity with oxygen plasma treatment, J. Phys. Chem. C 115 (37) (2011) 18213–18220.
[21] D.K. Sarkar, N. Saleema, One-step fabrication process of superhydrophobic green coatings, Surf. Coat. Technol. 204 (15) (2010) 2483–2486.
[22] L.B. Boinovich, A.M. Emelyanenko, V.K. Ivanov, A.S. Pashinin, Durable icephobic coating for stainless steel, ACS Appl. Mater. Interfaces 5 (7) (2013) 2549–2554.
[23] S.H. Park, E.H. Cho, J. Sohn, P. Theilmann, K. Chu, S. Lee, et al., Design of multi-functional dual hole patterned carbon nanotube composites with superhydrophobicity and durability, Nano Res. 6 (6) (2013) 389–398.
[24] Y.M. Zheng, H. Bai, Z.B. Huang, X.L. Tian, F.Q. Nie, Y. Zhao, et al., Directional water collection on wetted spider silk, Nature 463 (7281) (2010) 640–643.
[25] Y. He, C.Y. Jiang, P.J. Hu, R.Y. Yang, W. Tian, W.Z. Yuan, Reducing ice accumulation and adhesion by using a flexible micro-rod film, Cold Reg. Sci. Technol. 118 (2015) 57–63.
[26] Q.Y. Wang, G. Sun, Q.D. Tong, W. Yang, W.T. Hao, Fluorine-free superhydrophobic coatings from polydimethylsiloxane for sustainable chemical engineering: preparation methods and applications, Chem. Eng. J. 426 (15) (2021).
[27] W.T. Hao, Y.N.Z. Zhong, Q. Yang, C.C. Ke, Y.S. Lu, W.P. Wang, Superhydrophobic and breathable polydimethylsiloxane/nano-SiO2@polylactic acid electrospun membrane with core-sheath fiber structure, PROG. ORG. COAT. 187 (2024) 108126.
[28] X.Z. Wang, X.B. Huang, Z.M. Ji, W.B. Hu, H.Q. Sheng, X.F. Li, Self-healing icephobic coating with UV shielding and removability based on biobased epoxy and reversible disulfide bonds, Polymer 283 (2023) 126274.
[29] X.Z. Wang, X.B. Huang, W.B. Hu, Z.M. Ji, H.Q. Sheng, H. Liu, Fluorine-free, highly transparent, chemically durable and low ice adhesion icephobic coatings from biobased epoxy and polydimethylsiloxane, JAPS 140 (6) (2023) e53456.
[30] S.Q. Hong, R.T. Wang, W.B. Hu, H. Liu, Facile one-step fabrication of PHC/PDMS anti-icing coatings with mechanical properties and good durability, PROG. ORG. COAT. 135 (2019) 263–269.
[31] Y.B. Liu, Y. Wu, S.J. Liu, et al., Material strategies for ice accretion prevention and easy removal, ACS Materials Lett 4 (2022) 246–262.
[32] M. Jung, T. Kim, H. Kim, F. Zhou, Design and fabrication of a large-area superhydrophobic metal surface with anti-icing properties engineered using a top-down approach, Appl. Surf. Sci. 351 (2015) 920–926.
[33] P. Yang, K. Yin, X. Song, L. Wang, Q. Deng, J. Pei, Y. He, C. Arnusch, Airflow triggered water film self-sculpturing on femtosecond laser-induced heterogeneously wetted micro/nanostructured surfaces, Nano Lett. 24 (2024) 3133–3141.
[34] M. Li, Y.C. Xiong, H.X. Wei, F.G. Yao, Y. Han, Y.J. Du, et al., Flexible Te/PEDOT: PSS thin films with high thermoelectric power factor and their application as flexible temperature sensors, Nanoscale 15 (2023) 11237–11246.
[35] J. Pei, K. Yin, T. Wu, L. Wang, Q. Deng, Y. Huang, et al., Multifunctional polyimide-based femtosecond laser micro/nanostructured films with triple Janus properties, Nanoscale 15 (2023) 15708–15716.
[36] H.Y. Wang, Z.J. Liu, E.Q. Wang, R.X. Yuan, D. Gao, X.G. Zhang, et al., A robust superhydrophobic PVDF composite coating with wear/corrosion-resistance properties, Appl. Surf. Sci. 332 (2015) 518–524.
[37] J. Guo, F.C. Yang, Z.G. Guo, Fabrication of stable and durable superhydrophobic surface on copper substrates for oil-water separation and ice-over delay, J. Colloid Interface Sci. 466 (2016) 36–43.
[38] S. Farhadi, M. Farzaneh, S.A. Kulinich, Anti-icing performance of superhydrophobic surfaces, Appl. Surf. Sci. 257 (14) (2011) 6264–6269.
[39] P. Tourkine, M.L. Merrer, D. Quéré, Delayed freezing on water repellent materials, Langmuir 25 (13) (2009) 7214–7216.
[40] V. Rico, J. Mora, P. García, Robust anti-icing superhydrophobic aluminum alloy surfaces by grafting fluorocarbon molecular chains, Appl. Mater. Today 21 (2020) 100815.
[41] W.M. Chen, X.Y. Zhou, X.T. Zhang, M. Feizbakhshan, Y.Z. Cao, S.K. Shi, et al., Fast formation of hydrophobic coating on wood surface via an energy-saving dielectric barrier discharges plasma, PROG. ORG. COAT. 125 (2018) 128–136.
[42] T. Hasegawa, T. Aizawa, T. Inohara, K. Wasa, M. Anzai, Hot mold stamping of optical plastics and glasses with transcription of super-hydrophobic surfaces, Procedia Manuf. 15 (2018) 1437–1444.
[43] S. Abrar, F. Nazeer, A. Malik, M. Kamal, A.G. Alsehemi, Ultra-low thermal conductivity and hydrophobic properties of high entropy β-type quaternary pyrosilicate, J. Eur. Ceram. Soc. 3 (2024) 1698–1709.
[44] Z.L. Jin, X.T. Chen, Y.Q. Wang, D.B. Wang, Thermal conductivity of PTFE composites filled with graphite particles and carbon fibers, Comp. Mater. Sci. 102 (2015) 45–50.
[45] S.T. Xu, Y.H. Sun, X.S. Lü, Q.C. Yang, Q. Li, Z.D. Wang, et al., Effects of composition and pore evolution on thermophysical properties of Huadian oil shale in retorting and oxidizing pyrolysis, Fuel 305 (2021) 121565.
[46] A. Alizadeh, M. Yamada, R. Li, W. Shang, S. Otta, S. Zhong, et al., Dynamics of ice nucleation on water repellent surfaces, Langmuir 28 (6) (2012) 3180–3186.
[47] X.L. Zhan, Y.D. Yan, Q.H. Zhang, F.Q. Chen, A novel superhydrophobic hybrid nanocomposite material prepared by surface-initiated AGET ATRP and its anti-icing properties, J. Mater. Chem. A 2 (24) (2014) 9390–9399.
[48] Q. He, Y. Xu, F.Y. Zhang, Y.Y. Jia, Z.C. Du, G.T. Li, et al., Preparation methods and research progress of super-hydrophobic anti-icing surface, Adv. Colloid Interface Sci. 323 (2024) 103069.
[49] K. Shi, X.L. Duan, Freezing delay of water droplets on metallic hydrophobic surfaces in a cold environment, Appl. Therm. Eng. 216 (2022) 119131.
[50] Q.T. Fu, X.H. Wu, D. Kumar, J.W.C. Ho, P.D. Kanhere, N. Srikanth, et al., Development of sol-gel icephobic coatings: effect of surface roughness and surface energy, ACS Appl. Mater. Interfaces 6 (23) (2014) 20685–20692.
[51] T. Bharathidasan, S. Vijay Kumar, M.S. Bobji, R.P.S. Chakradhar, B.J. Basu, Effect of wettability and surface roughness on ice-adhesion strength of hydrophilic, hydrophobic and superhydrophobic surfaces, Appl. Surf. Sci. 314 (2014) 241–250.
[52] X.H. Wu, Y.Z. Shen, S.L. Zheng, Z.T. Hu, Z. Chen, Clarifying the correlation of ice adhesion strength with water wettability and surface characteristics, Langmuir 36 (41) (2020) 12190–12201.
[53] J. Soltis, J. Palacios, T. Eden, D. Wolfe, Evaluation of ice-adhesion strength on erosion-resistant materials, AIAA J. 53 (7) (2015) 1825–1835.
[54] Z.A. Janjua, The influence of freezing and ambient temperature on the adhesion strength of ice, Cold Reg. Sci. Technol. 140 (2017) 14–19.
[55] Q. Zhao, Y. Liu, E.W. Abel, Effect of temperature on the surface free energy of amorphous carbon films, J. Colloid Interface Sci. 280 (1) (2004) 174–183.
[56] T. Bharathidasan, S.V. Kumar, M.S. Bobji, R.P.S. Chakradhar, B.J. Basu, Effect of wettability and surface roughness on ice-adhesion strength of hydrophilic, hydrophobic and superhydrophobic surfaces, Appl. Surf. Sci. 314 (1) (2014) 241–250.
[57] Y.L. Zhan, M. Ruan, W. Li, H. Li, L.Y. Hu, F.M. Ma, et al., Fabrication of anisotropic PTFE superhydrophobic surfaces using laser microprocessing and their self-cleaning and anti-icing behavior, Colloids Surf. A Physicochem. Eng. Asp. 535 (2017) 8–15.
[58] X.T. Chang, M.Y. Li, S.K. Tang, L. Shi, X.Q. Chen, S.C. Niu, et al., Superhydrophobic micro-nano structured PTFE/WO3 coating on low-temperature steel with outstanding anti-pollution, anti-icing, and anti-fouling performance, SURF. COAT. TECH. 434 (2022) 128214.
[59] M. Xu, Z. Wang, L. Guo, L.M. Tao, T.B. Ma, T.M. Wang, et al., Tribological properties of PTFE-based fabric composites at cryogenic temperature, FRICTION 12 (2024) 245–257.
[60] E. Lozowski, K. Szilder, L. Poirier, A bobsleigh ice friction model, Int. J. Offshore Polar Eng. 24 (1) (2014) 52–60.